crystals

MDPI

Article

High-Performance Nanoplasmonic Enhanced Indium Oxide—UV Photodetectors

Eric Y. Li [1], Andrew F. Zhou [2,*] and Peter X. Feng [1,*]

[1] Department of Physics, University of Puerto Rico, San Juan, PR 00936, USA
[2] Department of Chemistry, Biochemistry, Physics, and Engineering, Indiana University of Pennsylvania, Indiana, PA 15705, USA
* Correspondence: fzhou@iup.edu (A.F.Z.); peter.feng@upr.edu (P.X.F.)

Abstract: In this paper, high-performance UV photodetectors have been demonstrated based on indium oxide (In_2O_3) thin films of approximately 1.5–2 μm thick, synthesized by a simple and quick plasma sputtering deposition approach. After the deposition, the thin-film surface was treated with 4–5 nm-sized platinum (Pt) nanoparticles. Then, titanium metal electrodes were deposited onto the sample surface to form a metal–semiconductor–metal (MSM) photodetector of 50 mm^2 in size. Raman scattering spectroscopy and scanning electron microscope (SEM) were used to study the crystal structure of the synthesized In_2O_3 film. The nanoplasmonic enhanced In_2O_3-based UV photodetectors were characterized by various UV wavelengths at different radiation intensities and temperatures. A high responsivity of up to 18 A/W was obtained at 300 nm wavelength when operating at 180 °C. In addition, the fabricated prototypes show a thermally stable baseline and excellent repeatability to a wide range of UV lights with low illumination intensity when operating at such a high temperature.

Keywords: UV photodetectors; surface functionalization; indium oxide; nanoplasmonic

Citation: Li, E.Y.; Zhou, A.F.; Feng, P.X. High-Performance Nanoplasmonic Enhanced Indium Oxide—UV Photodetectors. *Crystals* **2023**, *13*, 689. https://doi.org/10.3390/cryst13040689

Academic Editor: Alessandro Chiasera

Received: 23 March 2023
Revised: 12 April 2023
Accepted: 14 April 2023
Published: 17 April 2023

1. Introduction

Indium oxide (In_2O_3) has received much attention in multidisciplinary device applications such as flat-panel displays, light-emitting diodes (LEDs), and solar cells. Moreover, in recent years, indium oxide nanomaterials with different morphologies (nanoparticles, nanoflowers, nanosheets, nanowires, etc.) [1,2] have been found to be promising candidates for gas sensors [3–5]. On the other hand, indium oxide is a desirable material for developing smart, flexible, and wearable optoelectronics and multifunctional sensors in the field of environmental indicators [6], owing to its wide band gap (with reported values ranging from 2.7 to 3.7 eV) [7], optical transparency, thermal and chemical resistance, flexibility and stretchability, ease of manufacturing and low fabrication cost. Hence, UV photodetectors (PDs) based on In_2O_3 nanostructures, such as nanowires [8–10], quantum dots [11], nanosheets [12], and nanoparticles [13], have been explored, which demonstrates that In_2O_3 is a candidate for developing UV PDs. However, there are neither reports on the UV photodetector based on In_2O_3 thin films, nor studies on PD performance comparison at different temperatures.

Recently, surface functionalization with noble metal nanoparticles (NPs, e.g., Au and Ag) was effectively used to improve ZnO [14], GaN [15] and UNCD [16] UV photodetector performances. The effects of different metals such as Pt, Al and Ag as well as nanoparticle size have been discussed in our previous publications [16–19]. The nanoplasmonic resonance in metal nanoparticles causes the strong absorption and scattering of incident light. As a result, the photodetector showed high responsivity, which is defined as the ratio of generated photocurrent and incident optical power. Although the surfaced functionalization of noble metal nanoparticles was demonstrated in indium oxide-based gas sensors [20],

to date, no papers have been published on surface functionalized In_2O_3 UV photodetectors with noble metal nanoparticles.

In the present work, we demonstrated a high-performance In_2O_3 UV photodetector with Pt nanoparticle surface functionalization. Pt nanoparticles were chosen due to their localized plasmon resonance featured in the UV region [21]. Very high responsivities have been obtained both at room temperature and an elevated temperature, which is much better than that of UV photodetectors with MSM (metal–semiconductor–metal) structures based on SiC [22], diamond [23], and oxides [24] that can operate at high temperatures. The fabricated prototypes show a thermally stable baseline and excellent repeatability to a wide range of UV lights with low illumination intensity.

2. Materials and Methods

Compared to metal–organic chemical vapor deposition (MOCVD) and molecular beam epitaxy (MBE) techniques, sputtering has features of a high deposition rate, low cost, acceptable quality of thin films, and capability to deposit on large-area substrates. Owing to these advantages and their flexibility in the control of composition and microstructure, magnetron sputtering is widely employed for the synthesis of various thin films. The In_2O_3 thin films used in this study were grown on Si (100) substrates under deposition durations of 15 min using a homemade RF reactive magnetron sputtering system [25] with a power of 200 W. The substrates were cleaned in acetone and methanol with ultrasonic vibration and then dried with blowing dry nitrogen gas before deposition. The target for the growth of In_2O_3 films was sintered In_2O_3 (99.9%), 2 -inch in diameter. The distance between the target and substrate was approximately 7–8 cm. All the films were deposited at room temperature and the obtained thickness of the sample was approximately 1.5–2.0 µm measured using a stylus surface profiler (DektakXT, BRUKER, Billerica, MA). After deposition, the samples were annealed at 400, 600 and 800 °C for 2 h, respectively. The base pressure of the chamber was on the order of 10^{-6} Torr and the working pressure with argon gas was maintained at approximately 8–10 mTorr. To enhance the responsivity of the In_2O_3 thin–film material to UV radiation, the samples were functionalized using platinum (Pt) nanoparticles before photodetector fabrication. The surface treatments with Pt nanoparticles lasted for 1–2 s by using a 200 W RF magnetron sputtering deposition technique.

3. Results and Discussions

SEM was utilized to generate high-resolution photographs of surface morphology, along with a Raman spectrometer enabling a deeper insight into structural information. Figure 1a–c show SEM images of three In_2O_3 samples after annealing at 400, 600 and 800 °C, respectively, for 2 h. The surfaces of the obtained samples are flat but many particles on the surface were clearly visible. Following an increase in the temperature on annealing, the sizes of these particles increased from the sub-micrometer range to approximately 1 micrometer. A tentative interpretation is that melting and dissociation of partial In_2O_3 thin films into droplets on the surfaces of the samples during annealing at very high temperatures results in a rough/coarse surface.

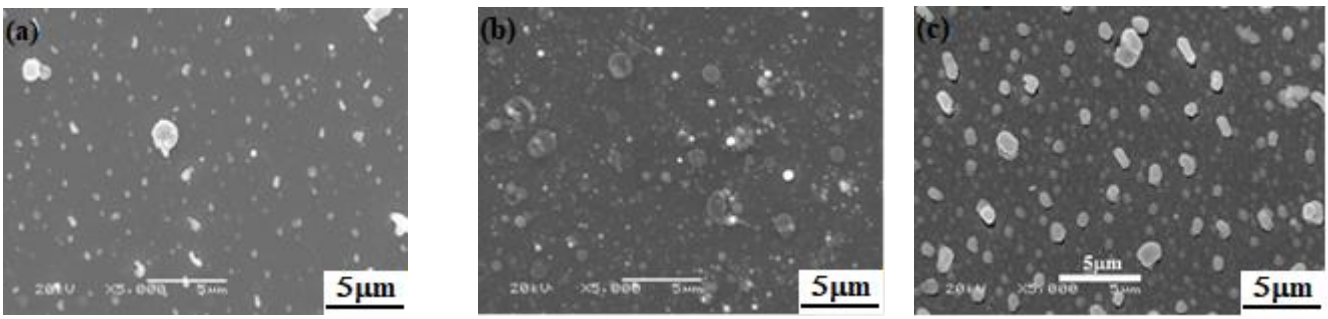

Figure 1. SEM images of In_2O_3 samples annealed at (**a**) 400 °C, (**b**) 600 °C, and (**c**) 800 °C, respectively, for 2 h.

Generally, the coarse surface of sample-based devices would be seriously affected by the surrounding environment such as humidity or dust. Therefore, in the following part, the focus would be on the first sample (as shown in Figure 1a) annealed at 400 °C with better surface quality. As an n-type semiconductor, different preparation methods and conditions influence the crystalline structures of In_2O_3 synthesized, such as cubic or rhombohedral, although both have the same band gap energy. The body-centered cubic (bcc) In_2O_3 with lattice parameter a = 1.011 nm is the most stable structure that is preferred for electronic [26] applications due to its high conductivity.

The In_2O_3 films prepared for this study were characterized by room-temperature Raman spectroscopy. An Ar^+ ion laser (Model 95, Lexcel Laser Inc., Fremont, CA) with an excitation wavelength of 514 nm was used along with a triple-grating monochromator to measure the Raman spectra. The ~2 mW laser beam, after passing through an 80× Olympus microscope objective, was focused onto the sample surface with a spot size of 3~4 μm in diameter, corresponding to a laser power density of approximately 2×10^4 W/cm^2. It was noticed that at this power density, no obvious surface morphology change in the In_2O_3 samples was observed because of the annealing effect caused by the laser beam with an accumulation time of 30 s required by the Raman measurement. Figure 2 shows Raman spectra of In_2O_3 film deposited on Si(100) substrate before and after the surface treatment with platinum nanoparticles. As displayed in Figure 2, the strongest peak at approximately 521 cm^{-1} is from the Si substrate. The spectra from In_2O_3 are dominated by the optical phonon lines at 132, 307, 366, 495, and 627 cm^{-1}, corresponding to bcc In_2O_3. The narrow spectral lines at 132 and 307 cm^{-1} confirmed the good crystalline quality of the bcc In_2O_3 films.

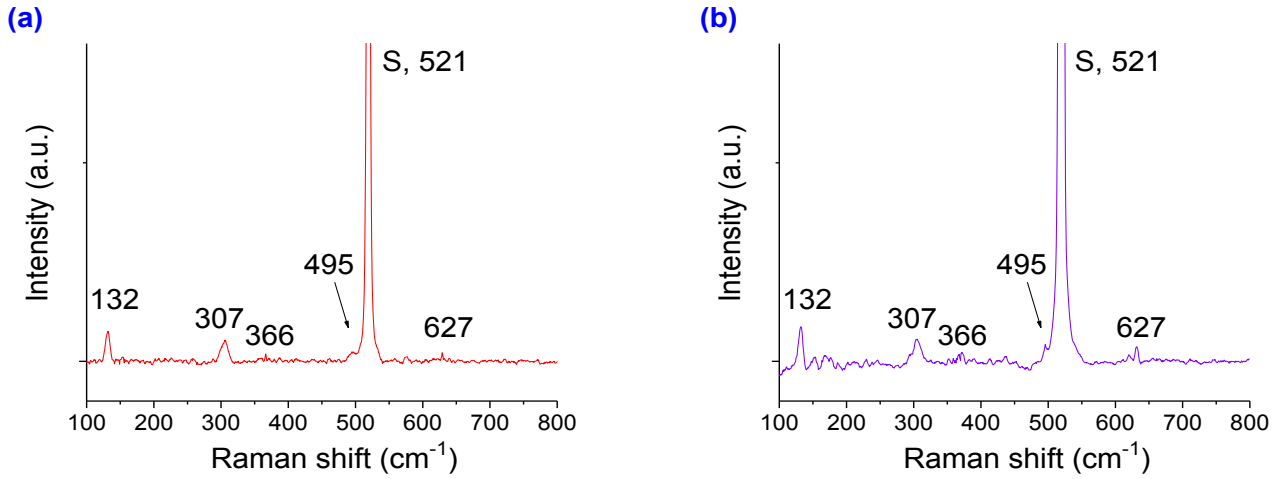

Figure 2. Raman scattering spectra of In_2O_3 thin film prepared on Si substrate (**a**) before and (**b**) after Pt treatment. The large peak at 521 cm^{-1} from the Si substrate is labeled as "S".

The fast fabrication process of the In_2O_3 thin-film-based photodetector is shown in Figure 3a. After the In_2O_3 thin film was deposited on Si(100) substrate, the sample surface was decorated with Pt nanoparticles. Then, a mask made of a metal wire of 400 μm in diameter was placed over the top surface of the In_2O_3 sample, followed by a 2-min direct coating of Ti metal electrodes of a thickness of 0.5–1 μm. The fabricated In_2O_3 UV photodetector was finally annealed at 200 °C for 60 min in the same vacuum chamber. Figure 3b shows the edge between the Ti electrode (grey) and In_2O_3 sensing material (black). The MSM geometry of the photodetector used in this investigation was similar to our previous boron nitride-based and SiC-based UV photodetectors [22,27] except for the In_2O_3 sensing layer. The gap formed by this simple and quick fabrication process was 400 μm between a pair of electrical electrodes, leading to a totally exposed surface area of 15 mm^2, although smaller gaps can be obtained with a more tedious lithography process.

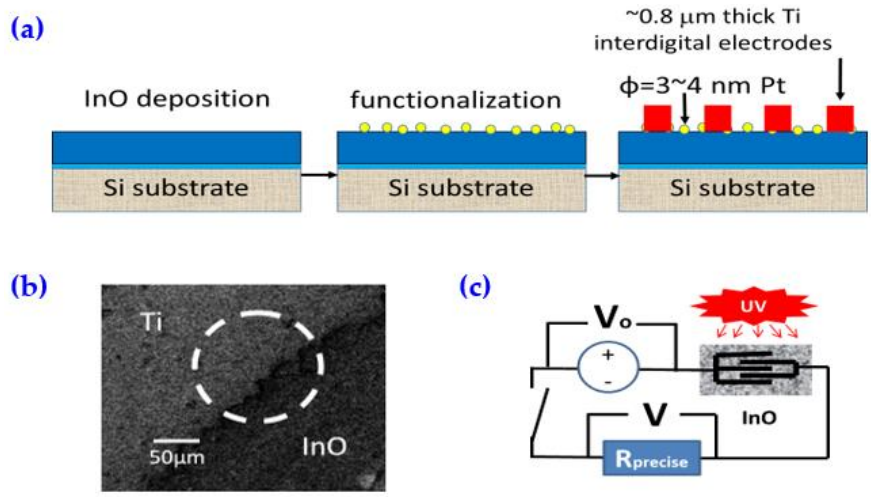

Figure 3. (**a**) Schematic diagram of the fabrication of the In_2O_3-based UV photodetector. (**b**) SEM image of the edge between the Ti electrode (grey) and sensing material (black) of the prototype. (**c**) Experimental setup for measuring electric properties and light responsivity of the UV photodetector.

Once the process flow of the MSM UV photodetector was completed, the prototypic UV photodetector was tested for its I–V graph and the photon-induced electrical current I_{ph} when the sensing material was exposed to UV radiation. As shown in Figure 3c, the prototype is connected in series with a precise resistor $R_{precise}$, a switch, and an Agilent voltage source power supply V_o. The voltage variations during the characterization across the precise resistor were monitored with a HEWLETT 34,401 electrical multimeter controlled by the LabVIEW program. To control the operating temperature of the tested prototype, a thermocouple and tungsten filament were deployed. The error of the measurements was approximately 5%.

The UV sensing mechanism of the In_2O_3 photodetector can be understood as a photoelectric phenomenon. As an n-type semiconductor, the conductivity of the In_2O_3 photodetector is largely due to the depletion region formed when there is no UV illumination because oxygen molecules trap free electrons to be ionized and chemisorbed on the surface. With UV radiation of photon energy slightly equal to or greater than the energy band gap of In_2O_3, the photoelectrically generated hole carriers recombine negatively charged adsorbed oxygen ions on the surface and discharge oxygen molecules that reduce the depletion region and increase the conductivity of the In_2O_3 sensing layer. Further illumination of UV light will generate more electron–hole pairs in the conduction and valence bands, which decreases the resistance significantly.

Figure 4a exhibits the four I–V graphs, i.e., the measured dark current as a function of the applied bias voltage when the prototype operates at room temperature (RT, 23 °C), 40 °C, 80 °C, and 120 °C, respectively, when the bias increases from zero to a maximum of 11 V. The linear relationship indicates a good ohmic contact formed between the electrode and the semiconductor except for a slightly curved I–V graph at room temperature. At room temperature, the unpaired electrons are collected at the anode under bias, which leads to a decrease in the width of the depletion layer. Therefore, an increase in conductivity occurs with an increase in the bias voltage. As a comparison, at room temperature, the dark current is approximately 28 μA at 4 V bias and 87 μA at 11 V.

The increase in dark current at higher temperatures is directly attributed to material properties. An increase in the operating temperature up to 40 and 80 °C results in an increase in the dark current to 42 μA and 80 μA at 4 V bias, respectively. With the increase in operating temperature, a lower resistance takes place with the departure of the chemisorbed oxygen molecules from the surface. As shown in Figure 4a, when biased at 4 V, the dark currents are 28, 43, and 80 μA for room temperature, 40 °C and 80 °C operation, respectively. When the temperature is high enough and the sample surface is already maintained in a chemisorbed oxygen molecule free or rather a dynamic equilibrium state, as indicated

by the I–V graphs at 80 °C and 120 °C in Figure 4a, further increase in the operating temperature does not boost the current. Similarly, as revealed in Figure 4b, the resistance of the device decreases with the increase in operating temperature. After the operating temperature reaches 80 °C, the resistance remains the same and no longer declines with the temperature rise.

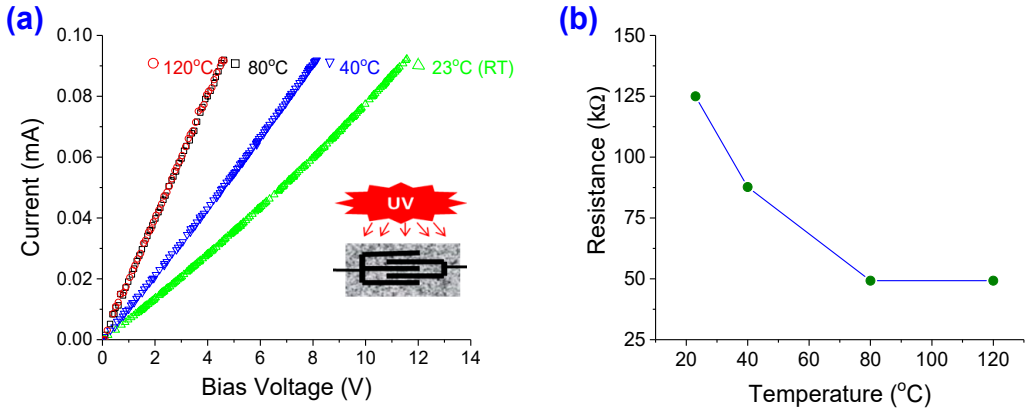

Figure 4. (**a**) Electrical current as a function of bias voltage at four different temperatures: room temperature (RT, 23 °C), 40 °C, 80 °C, and 120 °C. Inset: the schematic of the photodetector. (**b**) The temperature effect on the electrical resistance property of the In_2O_3 prototype.

To verify the authenticity of the photocurrent, the fabricated prototype was tested with UV light illuminations at different wavelengths for a period of 4 min and 50% duty, as shown in Figure 5. The device was operating at room temperature when the incident UV light intensity was 2 mW/cm^2 on the detector surface, which was controlled by varying the distance between the UV light source and the detector surface. As shown in Figure 5, the photocurrent rises and falls as the light is turned on and off when biased at 3.5 V. Besides, the device also displays good stability during the illumination cycle test. Under 250 nm, 300 nm, and 350 nm UV light illumination, the induced photocurrent is 0.39 mA, 0.48 mA, and 0.78 mA, respectively. At a longer wavelength, although the photocurrent is greater, the In_2O_3 prototype takes a longer time to respond. As indicated in Figure 5a,b, the measured photocurrent builds up quicker under 250 nm and 300 nm UV light, compared to 350 nm UV light illumination. On the other hand, noise under 250 nm UV light is greater than that under 300 nm and 350 nm UV light, since noise is greater at a short wavelength when the light intensity is fixed.

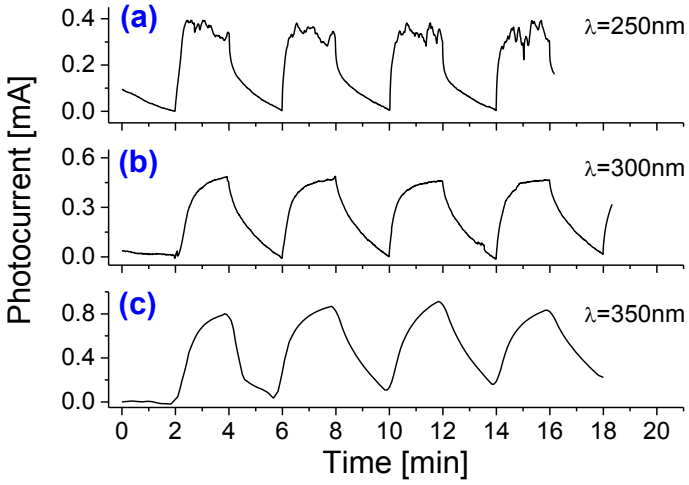

Figure 5. Photocurrent responding to 2 mW/cm^2 UV signals of a period of 4 min and a 50% duty cycle at (**a**) 250 nm, (**b**) 300 nm, and (**c**) 350 nm, respectively, when operating at room temperature and 3.5 V bias voltage.

Figure 6 shows the typical dependence of the photocurrent on UV light intensity under a bias of 3.5 V at room temperature. When the detector was exposed with a period of 4 min between the "switch-on" and "switch-off" to a 250 nm UV light at an intensity of 0.013 mW/cm^2, a well-defined light-induced photocurrent was obtainable with sharp edges. When the UV source was switched off, the photocurrent responded sharply down and then gradually decayed to zero. As expected, with the enhancement of illumination intensity, more electron-hole pairs are excited that contribute to the enriched photocurrent. As shown in Figure 6a–c, when exposed with the light intensities of 0.013, 0.17, and 2 mW/cm^2, the photocurrent measured are 0.10, 0.16 and 0.38 mA, respectively.

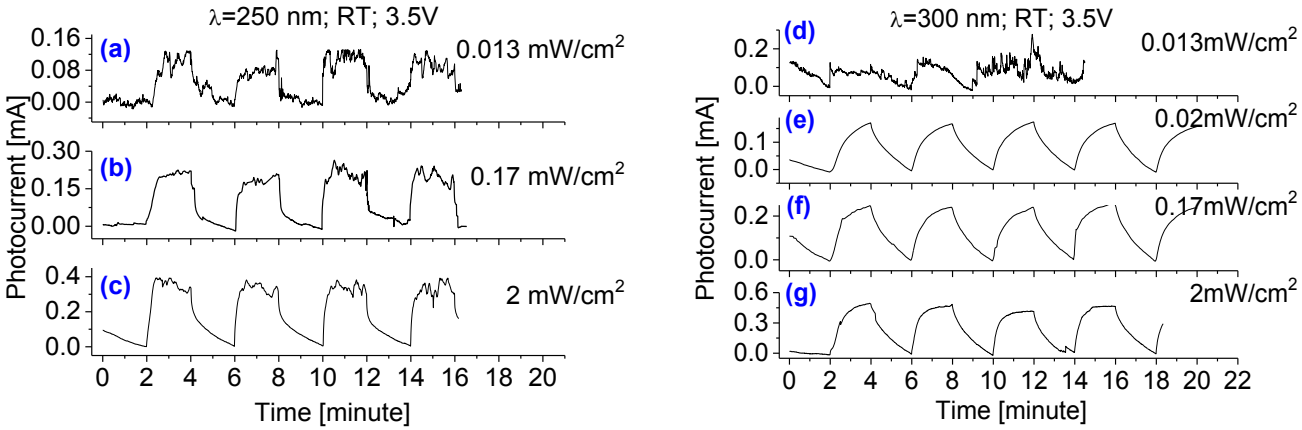

Figure 6. The measured photocurrents when illuminated with 250 nm of (**a**) 0.013 mW/cm^2, (**b**) 0.17 mW/cm^2, (**c**) 2 mW/cm^2, and when illuminated with 300 nm of (**d**) 0.013 mW/cm^2, (**e**) 0.02 mW/cm^2, (**f**) 0.17 mW/cm^2 and (**g**) 2 mW/cm^2, respectively. The device was operated at room temperature and biased at 3.5 V.

The photodetector's responsivity, R_λ, is defined as

$$R_\lambda = \frac{I_{ph}}{p_{light}}, \tag{1}$$

where I_{ph} is the maximal photocurrent from the detector, and P_{light} is the total incident light power on the surface of the detector. It can be estimated based on the experimental data. Since the exposed surface area of the detector is 15 mm^2, 250 nm light power on the surface of the detector at 13 μW/cm^2 intensity is approximately 1.95 μW, leading to a responsivity of 51 A/W at the bias of 3.5 V. When the intensities were increased to 0.17 mW/cm^2, and 2 mW/cm^2, the responsivity dropped to 6.3 A/W and 1.3 A/W, respectively. The reduction in responsivity under greater UV light intensity could be caused by the saturation of the sensing layer.

The external quantum efficiency (EQE), η, can be expressed by

$$\eta = R_\lambda \frac{hC}{\lambda q} \tag{2}$$

where h is Planck's constant, c the speed of light, q the electron charge, and λ the incident wavelength. A responsivity of 51 A/W at 250 nm corresponds to a quantum efficiency of 25.296% when operating at room temperature under an illumination intensity of 13 μW/cm^2 and a bias voltage of 3.5 V. We can also estimate the special detectivity D^* at this wavelength according to the following equation:

$$D^* = R_\lambda \sqrt{\frac{A}{2qI_d}}, \tag{3}$$

where I_d = 0.025 mA is the dark current at room temperature (Figure 4a). The calculated special detectivity is 7.0 × 10^{12} Jones at a power density of 13 μW/cm^2.

To find the photodetector's response at different UV wavelengths, 300 nm UV light was also used with different intensities ranging from 0.013, 0.02, 0.17 to 2 mW/cm^2, as shown in Figure 6d–g, corresponding to photocurrents of 0.1, 0.17, 0.24 and 0.46 mA, respectively. Higher photocurrents were obtained, compared to 250 nm UV light at the same intensities. The rise time and recovery time, on the other hand, were slightly longer than those under 250 nm wavelength UV light. Because of the MSM geometry, charge carriers generated close to the surface and top region can contribute to a fast rise time. While charge carriers generated further away from the surface must take extra time to diffuse to the electrodes, leading to a longer rise time. We believe that at 300 nm wavelength, the photocurrent of the prototype was dominated by the photo-generated charge carriers inside the layer rather than that from the surface, which travels a longer average distance, hence a longer rise time, to generate the current. Our observations also indicate that the absorption of 250 nm could be greater than that of 300 nm UV light. However, its lower responsivity at relatively greater illumination light intensity could be caused by the possible saturation due to its higher absorption. A trade-off should be made between the photocurrent and response time as the In_2O_3 layer thickness is optimized. The response of a device to different light illumination may also rely on the bandgap width or cross-section parameter of the active layer.

Since the temperature effect of In_2O_3 UV photodetectors has not been studied by other groups, it is interesting to see how an In_2O_3 UV photodetector behaves at different operating temperatures. Therefore, additional experiments have also been carried out and the photocurrents responding to 250 nm and 300 nm UV illumination when operated at room temperature, 180 °C and 300 °C are displayed in Figure 7. Under 250 nm UV light, with the increase in operating temperature from room temperature to 180 °C, the yielded photocurrent increases from 0.2 mA to 0.6 mA. However, the contribution of thermal noise to the obtained photocurrent increases too, as shown in Figure 7a–c. When the operating temperature was further raised to 300 °C, the photocurrent was completely buried under noise.

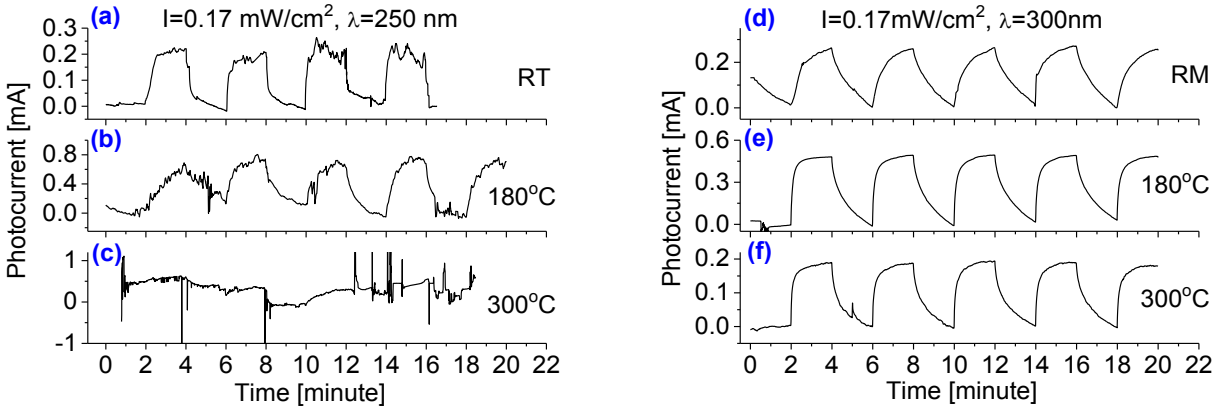

Figure 7. Photocurrents under UV light of 250 nm and 300 nm at an intensity of 0.17 mW/cm^2 with a period of 4 min at 50% duty cycle when operated at (**a**,**d**) room temperature (RT), (**b**,**e**) 180 °C, and (**c**,**f**) 300 °C. The bias voltage is 3.5 V.

As shown in Figure 7d–f, under 300 nm UV light of an intensity of 0.17 mW/cm^2, following the increase in temperature from 23 °C (RT) to 180 °C and then to 300 °C, the photocurrent was first increased from 0.28 mA to 0.47 mA and then decreased to 0.19 mA, giving a responsivity of 18 A/W at 180 °C and 7.3 A/W at 300 °C. The trend observed is similar to what was discovered with the In_2O_3-based oxygen sensors [28,29]. It is believed that with the temperature increase, apart from the resistance decrease due to the departure of adsorbed oxygen on the In_2O_3 surface, it is possible that the charge-carrier concentration increases, and the Debye length decreases and thus the sensitivity decreases [16].

The device also showed a faster response time and recovery time, and other good features such as excellent stability and repeatability, and a highly stable baseline when operating at both 180 and 300 °C. Upon receiving the UV light, the photocurrent reached its peak quickly and then dropped to zero gradually after the light source was switched off. The rise time, τ_r, which is defined as the interval from 10% to 90% of I_{max}, and fall time, τ_f, which is defined as the interval from 90% to 10% of I_{max}, are τ_r = 0.57 s and τ_f = 1.4 s, respectively, when the device is irradiated with UV pulses. The short rise time is attributed to the Pt nanoparticle decoration and the low capacitance of the MSM geometry, although its responsivity is limited due to the small effective absorbing area caused by the metallization of the electrodes.

In fact, the noble metal nanoparticles deposited on a metal oxide semiconductor surface act as electron-hole separators to promote the interfacial charge-transfer kinetics between the metal and semiconductor as reported in [14]. For example, the Ag-nanoparticle-decorated ZnO nanowire-based UV photodetector effectively eliminated the common persistent photoconductivity effect, leading to a significant decrease in the rise time as well as the dark current. However, the relatively long fall time is possible owing to the well-known persistent photoconductivity (PPC) effect in metal oxide nanostructure-based UV photodetectors, governed by the presence of numerous trapping states at crystal defects and the depth of the trap that prevent the photogenerated minority carriers from recombination and prolong the recovery time. As a comparison, Table 1 outlines the reported performance parameters of UV photodetectors operating at elevated temperatures.

Table 1. Comparison of the key device performance of the reported UV photodetectors.

Material	Peak λ (nm)	Responsivity (A/W)	Bias Voltage (V)	Response Time	Temperature Tested (°C)	Ref
SiC	250	0.1	10	18 s	180	[22]
Diamond	350	2.0	0	< 1 s	RT	[23]
TiO_2	220	0.2	30	20 μs	RT	[24]
In_2O_3 quantum dots	290	70	5	-	RT	[11]
In_2O_3 nanosheets	254	0.172	-	-	RT	[12]
In_2O_3 nanoparticles	340	11	20	500 s	RT	[13]
In_2O_3 film	300	18	3.5	0.57 s	180	This work

4. Conclusions

In_2O_3 thin films were synthesized on Si substrates using the RF sputtering technique, followed by the surface decoration of Pt nanoparticles. The Raman spectroscopy measurements confirmed that the thin films consisted of crystalline cubic In_2O_3. Finally, an MSM UV photodetector was fabricated using a simple and low-cost approach. The synthesis of a thin-film layer used for the UV photodetector eliminated the tight control needed for a nanostructure counterpart. Furthermore, there was no requirement for an expansive photolithography process in the device fabrication. A high responsivity to a wide range of UV light from 250 to 350 nm was demonstrated for the fabricated photodetector, as well as good stability and repeatability. When operated with a 3.5 V bias at room temperature, a responsivity of 50 A/W was achieved at 250 nm wavelength. Following a slight increase in the operating temperature, the fabricated photodetector runs well with improved responsivity, stability, and repeatability, as well as a faster rise time and fall time. However, a further increase in operating temperature would eventually lead to high thermal noise that dominates the output. The obtained experimental data indicated that at under 300 nm radiation, the best performance was achieved at 180 °C although the device was still working properly at temperatures up to 300 °C. This characteristic is much better than that of UV photodetectors based on other materials that were reported to operate at high temperatures but were generally limited to less than 150 °C. This experimental investigation suggests

that the simple approach described provides quick fabrication of high-performance UV photodetectors, which could possibly handle a high operating temperature of up to 300 °C.

Author Contributions: Designing and performing the experiments, as well as analyzing the data and writing this manuscript, E.Y.L., A.F.Z. and P.X.F. All authors have read and agreed to the published version of the manuscript.

Funding: NSF-CREST Center for Innovation, Research and Education in Environmental Nanotechnology (CIRE2N), grant HRD-1736093.

Data Availability Statement: Not applicable.

Acknowledgments: This work was financially supported by the NSF-CREST Center for Innovation, Research and Education in Environmental Nanotechnology (CIRE2N), grant HRD-1736093. A.F.Z. acknowledges the receipt of an IUP USRC research grant award.

Conflicts of Interest: The authors declare no conflict of interest.

References

1. Gu, F.; Li, C.; Han, D.; Wang, Z. Manipulating the defect structure (VO) of In_2O_3 nanoparticles for enhancement of formaldehyde detection. *ACS Appl. Mater. Interfaces* **2018**, *10*, 933–942. [CrossRef]
2. Zhao, S.; Shen, Y.; Zhou, P.; Hao, F.; Xu, X.; Gao, S.; Wei, D.; Ao, Y.; Shen, Y. Enhanced NO_2 sensing performance of ZnO nanowires functionalized with ultra-fine In2O3 nanoparticles. *Sens. Actuators B Chem.* **2020**, *308*, 127729. [CrossRef]
3. Wang, C.; Chen, D.; Jiao, X.; Chen, C. Lotus-root-like In_2O_3 nanostructures: Fabrication, characterization, and photoluminescence properties. *J. Phys. Chem. C* **2007**, *111*, 13398–13403. [CrossRef]
4. Staerz, A.; Weimar, U.; Barsan, N. Current state of knowledge on the metal oxide based gas sensing mechanism. *Sens. Actuators B Chem.* **2022**, *358*, 131531. [CrossRef]
5. Liu, W.; Xie, Y.; Chen, T.; Lu, Q.; Rehman, S.U.; Zhu, L. Rationally designed mesoporous In_2O_3 nanofibers functionalized Pt catalysts for high-performance acetone gas sensors. *Sens. Actuators B Chem.* **2019**, *298*, 126871. [CrossRef]
6. Yoon, Y.; Truong, P.L.; Lee, D.; Ko, S.H. Metal-oxide nanomaterials synthesis and applications in flexible and wearable sensors. *ACS Nanosci. Au* **2021**, *2*, 64–92. [CrossRef]
7. Bierwagen, O. Indium oxide—A transparent, wide-band gap semiconductor for (opto)electronic applications. *Semicond. Sci. Technol.* **2015**, *30*, 024001. [CrossRef]
8. Zhang, D.; Li, C.; Han, S.; Liu, X.; Tang, T.; Jin, W.; Zhou, C. Ultraviolet photodetection properties of indium oxide nanowires. *Appl. Phys. A* **2003**, *77*, 163–166. [CrossRef]
9. Meng, M.; Wu, X.; Ji, X.; Gan, Z.; Liu, L.; Shen, J.; Chu, P.K. Ultrahigh quantum efficiency photodetector and ultrafast reversible surface wettability transition of square In_2O_3 nanowires. *Nano Res.* **2017**, *10*, 2772–2781. [CrossRef]
10. Meng, M.; Yang, L.; Wu, X.; Gan, Z.; Pan, W.; Liu, K.; Li, C.; Qin, N.; Li, J. Boosted photoelectrochemical performance of In_2O_3 nanowires via modulating oxygen vacancies on crystal facets. *J. Alloys Compd.* **2020**, *845*, 156311. [CrossRef]
11. Rajamani, S.; Arora, K.; Konakov, A.; Belov, A.; Korolev, D.; Nikolskaya, A.; Mikhaylov, A.; Surodin, S.; Kryukov, R.; Nikolitchev, D.; et al. Deep UV narrow-band photodetector based on ion beam synthesized indium oxide quantum dots in Al_2O_3 matrix. *Nanotechnology* **2018**, *29*, 305603. [CrossRef] [PubMed]
12. Zhang, M.; Yu, H.; Li, H.; Jiang, Y.; Qu, L.; Wang, Y.; Gao, F.; Feng, W. Ultrathin In_2O_3 Nanosheets toward High Responsivity and Rejection Ratio Visible-Blind UV Photodetection. *Small* **2023**, *19*, 2205623. [CrossRef] [PubMed]
13. Shao, D.; Qin, L.; Sawyer, S. Near ultraviolet photodetector fabricated from polyvinyl-alcohol coated In_2O_3 nanoparticles. *Appl. Surf. Sci.* **2012**, *261*, 123–127. [CrossRef]
14. Tzeng, S.K.; Hon, M.H.; Leu, C. Improving the performance of a zinc oxide nanowire ultraviolet photodetector by adding silver nanoparticles. *J. Electrochem. Soc.* **2012**, *159*, H440. [CrossRef]
15. Li, D.; Sun, X.; Song, H.; Li, Z.; Chen, Y.; Jiang, H.; Miao, G. Realization of a high-performance GaN UV detector by nanoplasmonic enhancement. *Adv. Mater.* **2012**, *24*, 845–849. [CrossRef]
16. Zhou, A.F.; Velázquez, R.; Wang, X.; Feng, P.X. Nanoplasmonic 1D diamond UV photodetectors with high performance. *ACS Appl. Mater. Interfaces* **2019**, *11*, 38068–38074. [CrossRef]
17. Chu, J.; Peng, X.; Sajjad, M.; Yang, B.; Feng, P.X. Nanostructures and sensing properties of ZnO prepared using normal and oblique angle deposition techniques. *Thin Solid Film.* **2012**, *520*, 3493–3498. [CrossRef]
18. Zhou, A.F.; Wang, X.; Pacheco, E.; Feng, P.X. Ultrananocrystalline Diamond Nanowires: Fabrication, Characterization, and Sensor Applications. *Materials* **2021**, *14*, 661. [CrossRef]
19. Aldalbahi, A.; Velázquez, R.; Zhou, A.F.; Rahaman, M.; Feng, P.X. Bandgap-Tuned 2D Boron Nitride/Tungsten Nitride Nanocomposites for Development of High-Performance Deep Ultraviolet Selective Photodetectors. *Nanomaterials* **2020**, *10*, 1433. [CrossRef]
20. Kim, S.S.; Park, J.Y.; Choi, S.W.; Kim, H.S.; Na, H.G.; Yang, J.C.; Kim, H.W. Significant enhancement of the sensing characteristics of In_2O_3 nanowires by functionalization with Pt nanoparticles. *Nanotechnology* **2010**, *21*, 415502. [CrossRef]

21. Zhang, X.; Liu, Q.; Liu, B.; Yang, W.; Li, J.; Niu, P.; Jiang, X. Giant UV photoresponse of a GaN nanowire photodetector through effective Pt nanoparticle coupling. *J. Mater. Chem. C* **2017**, *5*, 4319–4326. [CrossRef]
22. Aldalbahi, A.; Li, E.; Rivera, M.; Velazquez, R.; Altalhi, T.; Peng, X.; Feng, P.X. A new approach for fabrications of SiC based photodetectors. *Sci. Rep.* **2016**, *6*, 1–10. [CrossRef]
23. Pacheco, E.; Zhou, B.; Aldalbahi, A.; Zhou, A.F.; Feng, P.X. Zero-biased and visible-blind UV photodetectors based on nitrogen-doped ultrananocrystalline diamond nanowires. *Ceram. Int.* **2022**, *48*, 3757–3761. [CrossRef]
24. Liu, Z.; Li, F.; Li, S.; Hu, C.; Wang, W.; Wang, F.; Lin, F.; Wang, H. Fabrication of UV photodetector on TiO2/diamond film. *Sci. Rep.* **2015**, *5*, 14420. [CrossRef] [PubMed]
25. Feng, P.X.; Aldalbahi, A. A compact design of a characterization station for far UV photodetectors. *Rev. Sci. Instrum.* **2018**, *89*, 015001. [CrossRef] [PubMed]
26. Eranna, G. *Metal Oxide Nanostructures as Gas Sensing Devices*; CRC Press: Boca Raton, FL, USA, 2011; pp. 1–336.
27. Rivera, M.; Velázquez, R.; Aldalbahi, A.; Zhou, A.F.; Feng, P.X. UV photodetector based on energy bandgap shifted hexagonal boron nitride nanosheets for high-temperature environments. *J. Phys. D Appl. Phys.* **2018**, *51*, 045102. [CrossRef]
28. Neri, G.; Bonavita, A.; Micali, G.; Rizzo, G.; Pinna, N.; Niederberger, M. In_2O_3 and Pt-In_2O_3 nanopowders for low temperature oxygen sensors. *Sens. Actuators B Chem.* **2007**, *127*, 455–462. [CrossRef]
29. Rumyantseva, M.N.; Makeeva, E.A.; Badalyan, S.M.; Zhukova, A.A.; Gaskov, A.M. Nanocrystalline SnO_2 and In_2O_3 as materials for gas sensors: The relationship between microstructure and oxygen chemisorption. *Thin Solid Film.* **2009**, *518*, 1283–1288. [CrossRef]